Journal of Vibration and Control
():2–17

DOI: 10.1177/ToBeAssigned
www.sagepub.com/
SAGE

Experimental Evidence of Hopf Bifurcation Induced by Wing–Wing Interaction in Flapping Flight

Dipan Deb[1], Kevin Huang[1], Moatasem Fouda[1], and Haithem E. Taha[1]

Abstract

The current study presents the transition of large amplitude oscillations to a fixed hovering point in the context of Bio-inspired flapping robots (BIFRs). The experimental arrangement allows two degrees of freedom for the BIFRs under study: body pitching and translation. The primary objective of this investigation is to compare the flight mechanics characteristics of two almost-identical BIFR configurations: a two-winged configuration and a four-winged one that exploits wing-wing interaction for aerodynamic effects. A motion capture system is utilized to track the two degrees of freedom of each BIFR. The study reveals that the four-winged BIFR exhibits passive transition of large amplitude oscillations to a fixed point beyond a certain frequency, whereas no such transition was observed for the two-winged BIFR at any frequency within the considered range. Realizing that the main difference between the two systems lies within the wing-wing interaction, this study thus underscores the significance of the wing-wing interaction for the transitional response upon the four-winged model. This response might be due to a phenomenon called vibrational stabilization. From the study, it can be implied that wing-wing interaction promotes the transitional response beyond a critical frequency.

Keywords

Flapping flight, Wing–wing interactions, Motion capture, Bifurcation, Fixed-point transition

Introduction

In the last few decades, the Bio-inspired flapping flight has garnered a lot of attention from the aerodynamics, flight mechanics, and control communities. Although in the twentieth century, the main focus of flapping flight research was to understand the unsteady lifting mechanism (Ellington et al. 1996; Dickinson et al. 1999; Ellington and Lighthill 1984), in the twenty-first century, it moved towards efficient flapping flights (Taylor et al. 2003; Berman and Wang 2007; Ramananarivo et al. 2011). Researchers have put effort into optimizing some parameters to obtain higher efficiency for a given traditional flapping mechanism (Zheng et al. 2020; Chen et al. 2024). Another accepted way of increasing efficiency is a passive way; to exploit a non-traditional mechanism, such as the clapping effect facilitated by the wing-wing interaction (Armanini et al. 2016; Balta et al. 2021; Deb et al. 2023). The wing-wing interaction utilizes a stronger wingtip vortex Armanini et al. (2016) and an intensified jet effect Jadhav et al. (2019). Balta et al. (2021) demonstrated with flow visualization and force measurement that wing-wing interaction exploits this jet effect to passively enhance thrust generation. Deb et al. (2023) experimentally demonstrated how the jet effect actively enhances thrust during hovering. Furthermore, the bio-inspired flying robots (BIFRs) expose themselves to persistent oscillating aerodynamic forces. These oscillations are induced onto the body's motion in addition to its mean trajectory, which makes these vibrations self-induced. Intriguingly, it has been noted that these vibrations further enhance the performance of a four-winged flapping robot that enjoys wing-wing interaction (Deb et al. 2023, 2022)(e.g., Model B shown in Figure 1b 2b 3b). In contrast, these self-induced oscillations are detrimental to the conventional flapping mechanism (e.g. Model A shown in Figure 1a 2a 3a). However, in a real flight, stability is also a very important factor apart from enhanced efficiency.

It has been observed that in nature, e.g., the flapping flight of insects employs a passive stabilization mechanism, known as vibrational stabilization (Taha et al. 2015). This phenomenon was first observed in 1908 on an inverted pendulum (Stephenson 1908), and the underlying physics was revealed in 1951 by (Kapitza 1951). In this phenomenon, the unstable equilibrium is stabilized when subjected to a sufficiently fast vibration. Since then, numerous studies have been conducted to analyze and understand vibrational stabilization and control (Vela and Burdick 2003; Bullo 2002; Tahmasian and Woolsey 2015; Meerkov 1980; Hong 2002; Berg and Wickramasinghe 2015; Maggia et al. 2020). In flapping flight Taha et al. (2016); Hassan and Taha (2018) analytically assessed the

University of California, Irvine, California-92697, USA

Corresponding author:
Dipan Deb
Email: dipand@uci.edu

longitudinal flight stability near the hovering point of a flapping wing micro air-vehicle (FWMAV) by considering wing inertial effects and higher-order interactions. They were able to exhibit a negative pitch stiffness and a decrease in pitch damping due to the higher-order interactions and wing inertial dynamics. Along a similar line, Taha et al. (2020) employed chronological calculus to elucidate the utilization of vibrational stabilization in response to pitch perturbations by a hawkmoth during hovering. Moreover, by analyzing the interaction between the fast oscillatory aerodynamic loads on the wings and relatively slow body motion, Hassan and Taha (2019) showed a similar vibrational stabilization mechanism.

Furthermore, Taha et al. (2018) conducted experimental work in a two-degree-of-freedom bio-inspired flapping robot and utilized vibrational stabilization to explain their observation. This present study adopts a similar experimental configuration, employing a system characterized by two degrees of freedom, but comparing two flapping robots: (i) a two-winged robot designated as Model A, and (ii) a four-winged robot named Model B. Both models employ an identical crank-and-rocker mechanism for flapping and share the same wing material and geometry. The sole distinction between these robots resides within their aerodynamic characteristics. Model A (depicted in figures 1a, 2a, and 3a) employs a classical flapping mechanism, leveraging unsteady phenomena such as wake capture (Dickinson et al. 1999) and stable leading edge vortices (Sane 2003; Ellington et al. 1996) to generate aerodynamic forces. Conversely, Model B (illustrated in figures 1b, 2b, and 3b) strategically harnesses wing-wing interactions to enhance thrust production (Bennett 1977).

In the present study, the flight mechanics characteristics of these two flapping robots are compared at different flapping frequencies. As such, the effect of wing-wing interaction on the transitional behavior is assessed. The observed response of transition from high amplitude oscillations to a fixed point, might also be an example of antimonotonicity (Dawson et al. 1992; Bier and Bountis 1984). The only way the reason for the transition can be concluded is through a rigorous analytical exercise. However, this rigorous analysis heavily relies on the complex aerodynamics (shown in the equation of motion in the appendix), which could not be easily modeled due to the complex flow field and wing-wing interactions. Regardless, the transitional phenomenon underscores a favorable flight condition for the flapping flight with wing-wing interactions.

Experimental Method

Flapping Wing Models

Two different configurations of bio-inspired flapping robots are considered: (i) Model A, denoted as a two-winged flapping robot (figures 1a, 2a, 3a), and (ii) Model B, referred to as a four-winged flapping robot (figures 1b, 2b, 3b). Both flapping robots, Model A and Model B, are able to flap with a crank-rocker mechanism, which is also utilized by Balta et al. (2021) in the same laboratory. The leading edge rod is highlighted with red and the outline of the trailing edge is highlighted with yellow. The leading rod is

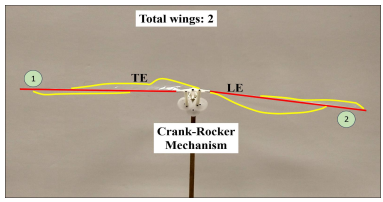

(a) Model A

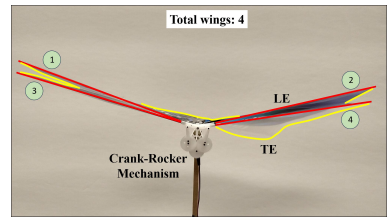

(b) Model B

Figure 1. Front view of the two BIFR configurations (Balta et al. 2021)

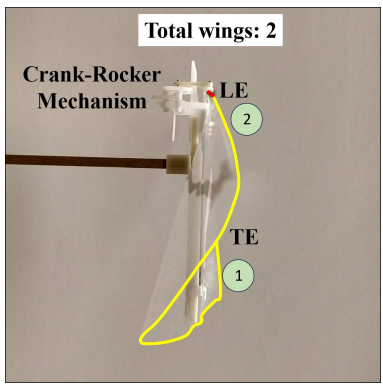

(a) Model A

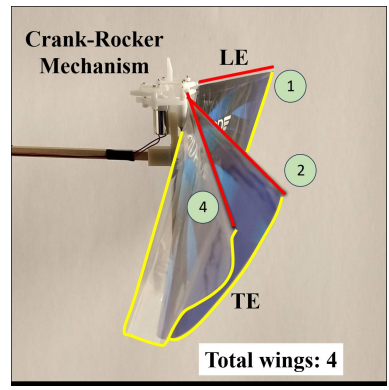

(b) Model B

Figure 2. View from the side of the FWMAVs (Balta et al. 2021)

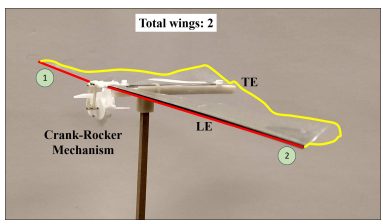

(a) Model A

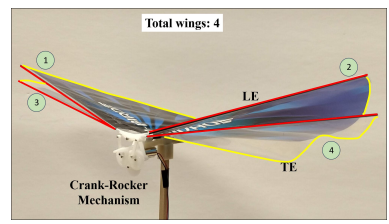

(b) Model B

Figure 3. An isometric view of the two BIFR configurations (Balta et al. 2021)

driven by the crank-rocker mechanism. The total number of wings for each model is shown and wings are numbered accordingly. The wing geometry is shown in Figure 4, with consistent color scheme for the leading edge (LE) and trailing edge (TE) as Figures 1, 2 & 3. The wing span of the leading edge (LE) is 140mm (denoted by R). The root chord of the wing is denoted by a, which is 95mm and the trailing edge (TE) is elliptical in shape. This wing geometry is consistent among all the models chosen for this study.

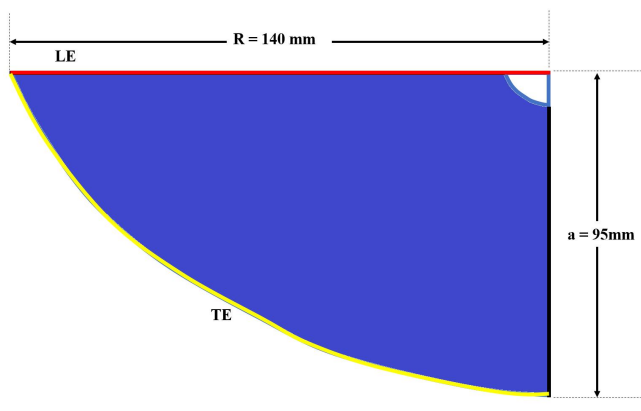

Figure 4. Wing Geometry

The crank-rocker mechanism drives the LE rod, which sets the wing in motion. More detail about this mechanism is provided in the appendix. The mechanism for generating aerodynamic forces fundamentally differs from Model A to B. While Model A (the two-winged robot) relies on a traditional lift generation mechanism via wing translation (i.e., translatory lift (Dickinson et al. 1999; Taha et al. 2012)), Model B exploits the wing-wing interaction (Balta et al. 2021; Armanini et al. 2016). Existing literature establishes that the wing-wing interaction inherently contributes to enhanced thrust during flapping flight (Bennett 1977; Phan et al. 2016). Thrust generation mechanisms for Model A & B are aerodynamically different (Balta et al. 2021; Deb et al. 2023). Consequently, it can be anticipated that the responses of the dynamical system will vary when tested with these distinct flapping mechanisms.

System Response Measurement

Figure 5 presents a schematic of the experimental setup used in the present work. The setup consists of a metallic frame (shown in light green), which serves as a mounting platform for the experimental setup. It is securely fixed to the laboratory floor. There is a pendulum rod (in yellow) mounted on hinge 'a'. The rod is allowed to rotate freely about the hinge, enabling it to swing like a regular pendulum. The pendulum angle between the pendulum rod and the vertical axis is denoted by γ. The BIFR (in blue) is mounted to the pendulum rod through a connecting rod (in green) at the hinge 'b' located on the robot as shown in Figure 5. The Figure also shows the approximate location of the center of mass (CM) of the flapping robot (in purple). The approximate location of the CM in the flapping robot frame is normalized by the body length (l_b) of it, $(d_g/l_b, h_g/l_b) \simeq (-0.37, -0.1)$. The change in CM due to the flapping of the wings can be neglected because the wings hold less than 1% of the robot mass. The body of the robot is free to rotate about this hinge. The body pitching angle between the BIFR body and the horizontal axis is denoted by θ. Whenever the robot flaps, depending on

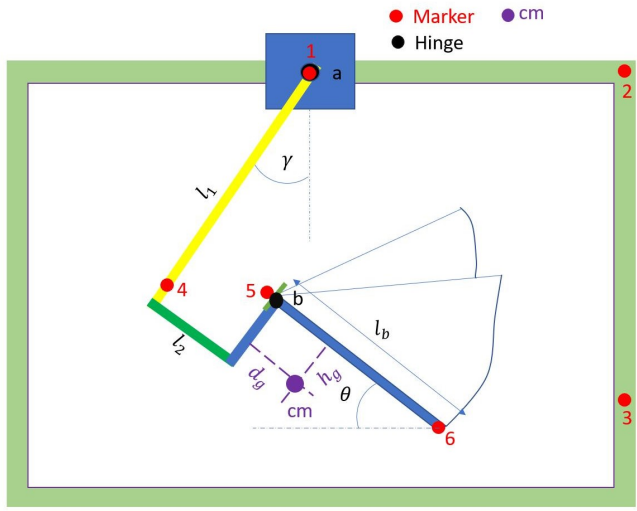

Figure 5. Schematic of the Experimental Setup with Marker locations

the frequency of flapping, γ and θ undergo oscillatory responses about certain average values. These angles provide valuable information about the behavior and dynamics of the system under study. The angle θ represents the pitching angle of an animal or a BIFR in free flight, and the angle γ mimics the translatory motion of the animal/BIFR. In fact, this reduced-degree-of-freedom setup is typical in the literature on helicopter stability and control (Dhiman et al. 2022).

In order to measure the angles synchronously, we have adopted a Motion capture system. This system consists of active markers and a tracker. The active markers are placed at the points of interest, and the tracker captures their positions in space over time. The accuracy of this system is remarkable, with spatial accuracy down to 0.1mm and temporal accuracy of $1\mu s$. Six markers (shown in red in Figure 5) are strategically placed for measurements. Markers 1, 2, and 3 are fixed orthogonally on the metallic frame, providing a stable reference. Marker 1, placed on the hinge 'a', along with marker 4, allows for the measurement of the angle γ. The angle θ is measured with the help of markers 5 and 6. The signals are acquired from the markers at 500 samples per second. In addition to the angles γ, θ, a hall sensor is utilized to measure the flapping frequency of the BIFR.

Results and Discussion

This section focuses on the main study of the paper about the stability characteristics of the two BIFR configurations at various flapping frequencies.

Unsteady Response of the BIFR models

This subsection discusses the transitional responses of Model A & B in terms of pendulum angle, γ, and body pitching angle, θ. Figure 6a shows the transitional system

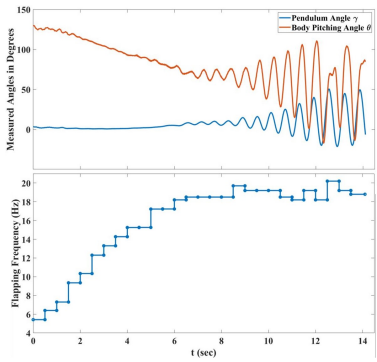

(a) Response of Model A in terms of the pendulum angle γ and the body pitching angle θ as the flapping frequency increases from a lower to a higher value. The increase in frequency with time is also shown in the bottom figure.

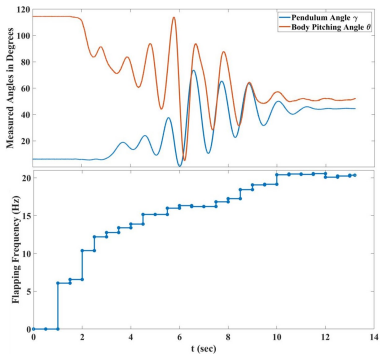

(b) Response of Model B in terms of the pendulum angle γ and the body pitching angle θ as the flapping frequency increases from zero to beyond the critical frequency. The increase in frequency with time is also shown in the bottom figure.

Figure 6. Unsteady system response of Model A & B with varied flapping frequencies

response of Model A. The increase in flapping frequency with time is also shown at the bottom. The frequency is calculated with a 0.5-second time interval. With the current methods utilized in this study, it is impossible to obtain a smooth frequency-time relation. Hence, the reported frequency is an interval-averaged value. The flapping frequency increases from about 5 Hz at $t = 0$ to about 20 Hz in almost $t = 14.5$ seconds. During this excursion, the system traverses into high amplitude oscillation with Model A. Similarly, Figure 6b shows the transitional response of the body and the pendulum angle for Model B as the flapping frequency increases from an inert state at $t = 2$ seconds to around 20 Hz. The high amplitude oscillations of Model A do not show any indication of abating, as shown in Figure 6a. In contrast, Figure 6b shows an evident transition into a fixed point $\{(\theta, \gamma) \sim (50°, 40°)\}$ at $t \sim 12$. This transition is observed beyond a critical flapping frequency (about 22 times the natural frequency of the system). It should be clarified that these two datasets show unsteady responses of the system, where the flapping frequency increases with time. The response at a given frequency is discussed in the later sections. Even while experimenting with steady flapping frequency, this fixed point transition is observed for Model B. However, this phenomenon is not observed in

Model A at any achievable frequency; this transitional behavior into a fixed point might be attributed to the effect of wing-wing interactions in flapping flight (Taha et al. 2015; Bullo 2002).

Natural Response of the Two BIFR Models

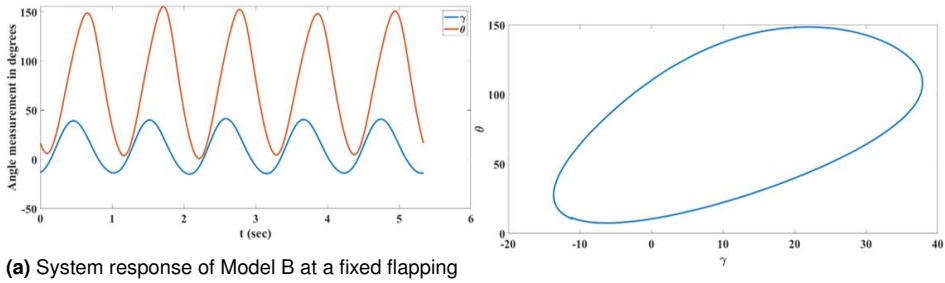

(a) System response of Model B at a fixed flapping frequency

(b) System response in $\theta - \gamma$ plane

Figure 7. System Response visualized with temporal change to $\theta - \gamma$ plane

The response of the system for different flapping frequencies and different models can be visualized differently. At some flapping frequencies, both models show large amplitude oscillations in the system. Figure 7 shows the system response for model B at $15.5Hz$ flapping frequency. Figure 7a shows the measurement of the body angle θ and the pendulum angle γ with respect to time. Whereas, figure 7b shows the same plot with phase average in the $\theta - \gamma$ plane. All the subsequent orbit plots are phase-averaged.

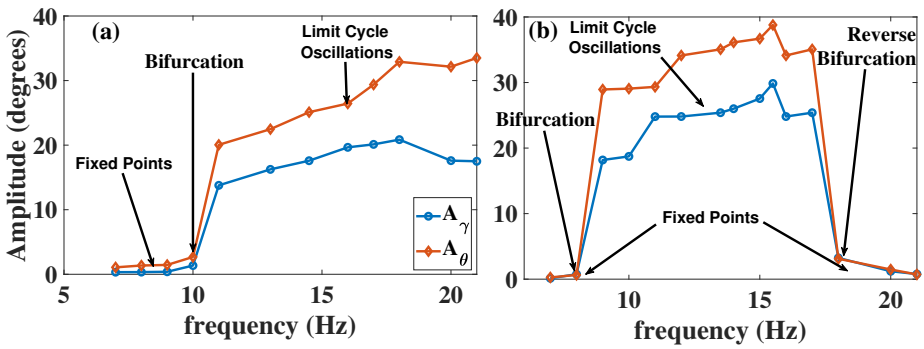

Figure 8. Evidence of Hopf Bifurcation (Hopf 1942) in the system response

Figure 8 shows the amplitudes of the limit cycle oscillations both in pendulum angle (γ) and the body angle (θ). Figure 8(a) shows the plot for Model A and Figure 8(b) depicts the response for Model B. The amplitudes of oscillation from the phase-averaged data are calculated as follows:

$$\begin{aligned} A_\gamma &= \frac{\gamma_{max} - \gamma_{min}}{2} \\ A_\theta &= \frac{\theta_{max} - \theta_{min}}{2} \end{aligned} \tag{1}$$

The amplitudes A_γ & A_θ are shown in Figure 8 in blue and orange respectively. For both models A & B it can be observed that at a very low frequency ($< 10Hz$ for Model A and $< 8Hz$ for Model B), there is no significant oscillation. This can also be observed in Figure 9 where the response at these very small frequencies appears to be fixed points in the $\theta - \gamma$ plane. As the flapping frequency increases, the system sets into high amplitude oscillation and the responses appear to be orbits at these frequencies. This is the point of Bifurcation shown in Figure 8. This can be an evidence for Hopf Bifurcation (Hopf 1942). However, for Model B a reverse bifurcation is observed beyond a frequency threshold ($f > 18Hz$) as shown in Figure 8. In this region, the high amplitude oscillations turn into small amplitude oscillations (almost a fixed point). This behavior is called antimonotonicity in literature (Dawson et al. 1992; Bier and Bountis 1984). However, there is no equivalent observation for model A.

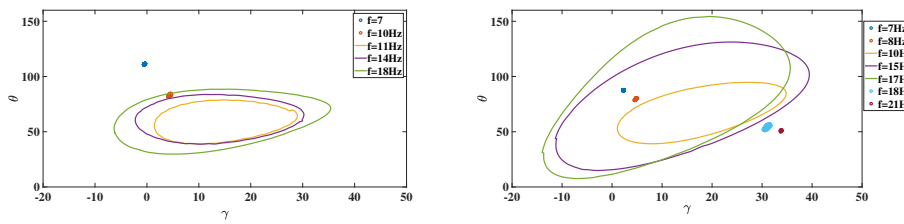

(a) Model A **(b)** Model B

Figure 9. System Response visualized in $\theta - \gamma$ plane at different flapping frequencies for both models

In the light of these findings, the behavior is found to be of a Hopf bifurcation type. As flapping frequency increases, the hovering fixed point transitions to a limit cycle of large amplitude, as shown in Figure 8. Moreover, for Model B, these limit cycles transition into fixed points, showing behavior of a reverse Hopf bifurcation type. Although these stable limit cycles may have an averaged attitude that is close to the fixed point, it is of too large amplitude to be acceptable for an insect or a micro air vehicle. A satisfactory hovering must be achieved by a minimal body oscillation amplitude.

Figure 9 shows a few examples of system responses of both models at a few flapping frequencies in the $\theta - \gamma$ plane. The arrows in both figures show the direction of increase in flapping frequency. Figure 9b shows the transition of high amplitude oscillations to a fixed point, for the flapping mechanism with wing-wing interaction.

Evidently, this discernible discrepancy in this comparative observation can be attributed to the wing-wing interaction. Despite their same crank and rocker mechanisms, wing geometry, and wing material, the pivotal variance lies in the aerodynamic response, particularly the wing-wing interaction within Model B. The aerodynamic characteristics due to the wing-wing interaction seem to be the driving factor behind the transition to a fixed-point equilibrium condition, observed in Model B, in contrast to Model A.

Stability of the Orbits

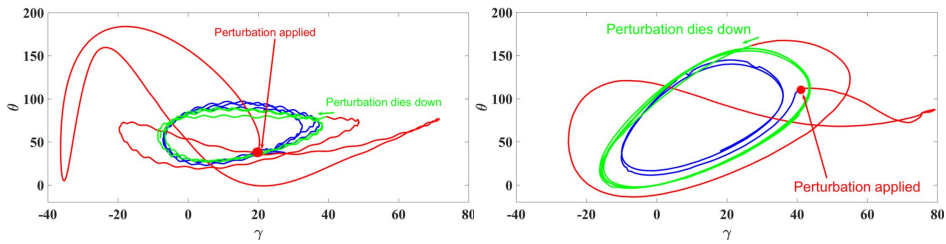

(a) Model A **(b)** Model B

Figure 10. Perturbation of the closed orbits

The response of the system in $\theta - \gamma$ plane can be shown as a closed orbit for a range of flapping frequencies for both Model A & B. The relatively large amplitudes of the pendulum and the body angle are responsible for this shape. Given the focus of this study on system stability, it is pertinent to evaluate the stability of these orbits. To investigate this, we introduced a perturbation to the orbit at a flapping frequency of 16 Hz, as illustrated in Figure 10. Figure 10a shows the system response to the applied perturbation for Model A and Figure 10b shows the same for Model B. The blue curve denotes the orbit before the application of the manual perturbation. The red curve shows the response of the system immediately after applying the perturbation. The red marker shows the point where the perturbation is applied and the green arrow shows the attenuation of the perturbation and the system returning to the limit cycle. The green arrow shows the orbit after the perturbation dies down. The perturbations were applied manually. Hence, it is not controlled or prescribed perturbations. However, after obtaining the data, the range of perturbations can be calculated. The conclusion of this perturbation study is based on the range of perturbations tabulated below. The perturbation range is normalized by the flapping frequency f at which they are applied.

Range	$\dot{\gamma}_{pert}/f$	$\dot{\theta}_{pert}/f$
Model A	$[1.4\ \ 39]$	$[7\ \ 237]$
Model B	$[1\ \ 10]$	$[3\ \ 342]$

Table 1. Flapping Angles for different Flapping Mechanisms

Although the large amplitude oscillation with the limit cycle is stable from a dynamical system perspective, the amplitude is too large for stable hovering. In this situation, the body of the BIFR deviates a significant amount from the hovering point. Hence, hovering in this case is deemed undesirable. However, the reverse transition from high amplitude oscillation to a fixed point hovering observed for Model B is desirable for stable hovering with minimal deviation.

Recovery of Model B from Various Perturbations

Upon achieving fixed point hovering beyond a flapping frequency for Model B, the system is subjected to various perturbations to study its qualitative recovery from these perturbations. Figure 11 & 12 shows the responses of the system in terms of $\gamma(t)$ and $\theta(t)$ after the application of different perturbations (initial conditions). All the perturbations are provided at around the flapping frequency of 20 Hz ($f \sim 20\ Hz$). At this frequency, the hovering point is about $(\bar{\theta}, \bar{\gamma}) \sim (55°, 30°)$.

Four different perturbations are considered. The system is subjected to angular perturbations both in body and pendulum angle, as presented in Figure 11. First, the flapping robot's body is set to a reduced angle ($\theta(0) < \bar{\theta}$) and subsequently released. The system restores its equilibrium in about 4 seconds, as shown in Figure 11a. A similar relatively fast recovery is observed when Model B is subjected to the second type of perturbation: the system is released at an initial pendulum angle larger than the equilibrium value (i.e., $\gamma(0) > \bar{\gamma}$), as shown in Figure 11b. Moreover, Figure 11a indicates that a significant perturbation in the body angle may not cause a significant influence on the pendulum angle. In contrast, Figure 11b shows that an initial disturbance in the pendulum angle γ may significantly impact the body pitching angle θ.

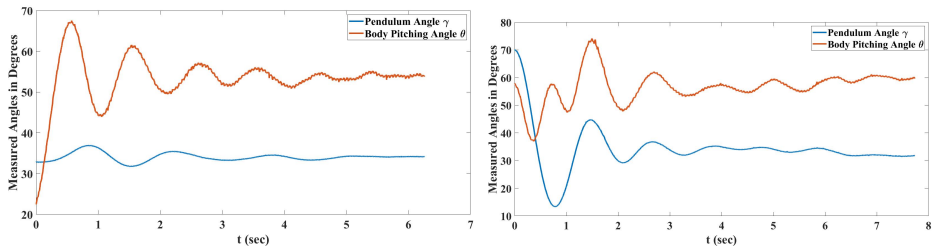

(a) System's Response Upon Release from Initial Body Angle

(b) System's Response Upon Release from Initial Pendulum Angle

Figure 11. Recovery of Model B from angular perturbations.

The other two perturbations considered in this work are concerned with applying an initial velocity (i.e., an impact) to the pendulum and the body as presented in Figure 12. Figure 12a shows the system's recovery from an initial body impact $\dot{\theta}(0) > 0$. Moreover, Figure 12b shows the system response after applying an impact on the pendulum $\dot{\gamma}(0) < 0$. It may be prudent to emphasize that these perturbations were applied manually, so uniformity was not the concern. Supplementary material provides video

recordings of the system's recovery in each case presented in Figure 11 & 12.Since the perturbations were applied manually, the quantification of the perturbations is not prescribed. However, it can be quantified during data analysis. For each trial, we calculate the perturbations as initial conditions $(\gamma_0, \theta_0,\ \dot{\gamma}_0,\ \dot{\theta}_0)$ and show them as a range in a table. The impact perturbations $(\dot{\gamma}_0,\ \dot{\theta}_0)$ are normalized by the flapping frequency f in the table. More details about these perturbations are provided in the appendix as supplementary material.

Perturbation	$\gamma_0 > \bar{\gamma}$	$\theta_0 > \bar{\theta}$ **or** $\theta_0 < \bar{\theta}$	$\dot{\gamma}_0/f < 0$	$\dot{\theta}_0/f > 0$
Range	$[54^\circ\ \ 70^\circ]$	$[22^\circ\ \ 134^\circ]$	$[-6.55\ \ -4.75]$	$[12.2\ \ 20.6]$

Table 2. Ranges of perturbations applied in the current study

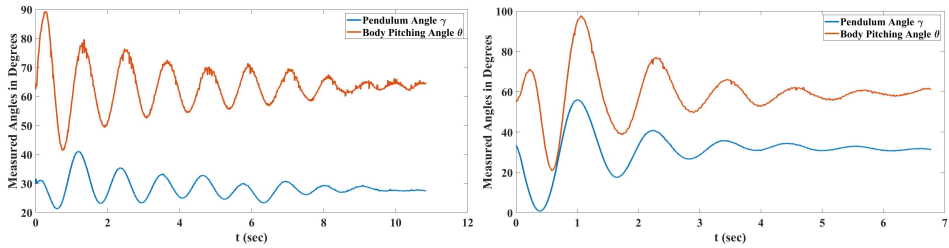

(a) System Behavior Following Body Impact Perturbation

(b) System Behavior Following Pendulum Impact Perturbation

Figure 12. Recovery of Model B from different pendulum perturbations.

One may ask whether the observed stability of Model B in comparison to Model A is due to vibrational stabilization (i.e., a higher-order effect that cannot be captured by direct averaging techniques). We believe that this is a possibility because it is achieved only beyond a certain frequency threshold (around 22 times the natural frequency of the system), which is typical in vibrational stabilization (Stephenson 1908; Kapitza 1951; Vela and Burdick 2003; Bullo 2002; Meerkov 1980; Taha et al. 2015, 2016; Hassan and Taha 2018, 2019; Taha et al. 2020, 2018). In contrast, our previous stability analysis using traditional averaging techniques indicated that the averaged system becomes more unstable as the frequency increases (Taha et al. 2014). In fact, at large mean angles of attack, the flapping counter torque mechanism (i.e., pitch damping) weakens as the flapping frequency increases (Bhatti et al. 2021; Taha 2013). So, these two facts may imply that the observed stability of model B at high frequencies is likely to be due to vibrational stabilization.

Finally, we would like to conclude by stating the main finding of this work: the stability of two almost-identical BIFRs, one with conventional flapping and another that exploits wing-wing interaction, was tested over a range of flapping frequencies. The latter exhibited a passive transition from large limit cycle oscillations to a fixed point, and the former did not. The two flappers have the same wing geometry, material, and motor, with

the only key difference in the wing-wing interaction. Hence, the wing-wing interaction may have a key role to play in the passive transition from a large amplitude limit cycle to a fixed point. Combined with our previous efforts by Hassan and Taha (2018) that showed the superiority of the wing-wing interaction BIFR over the traditional one in terms of thrust generation (Hassan and Taha 2018) and handling self-induced vibrations (Deb et al. 2023), one may conclude that the wing-wing interaction offers a very attractive design choice for bio-inspired flapping robots (Dickinson et al. 1999).

Highlights

These are the following highlights of this study

1. Wing-wing interaction may have a major role in transitioning from a large amplitude oscillation to a fixed point.
2. For bio-inspired flapping robots (BIFRs) whose wings experience considerable interaction, the hovering equilibrium experiences a natural (passive) transition to a favorable hovering condition, beyond a critical threshold of frequency.
3. In contrast, a dynamically-similar BIFR, whose wings do not enjoy significant wing-wing interactions, could not achieve the transition to a fixed point within the observed frequency range.

Conclusion

The present study is concerned with the effect of wing-wing interaction on a transitional phenomenon in flapping flight. For this purpose, we designed an experimental setup that allows only two degrees of freedom for the bio-inspired flapping robots (BIFR) under study: body pitching and translation. The stability characteristics of two almost identical BIFR configurations are experimentally tested. The first configuration, referred to as Model A, is a two-winged flapping robot that employs conventional flapping to generate aerodynamic forces. In contrast, the second configuration (Model B) is a four-winged robot, whose wing-wing interaction affects its aerodynamic force generation. At low flapping frequencies, both flapping robots exhibit high amplitude oscillations. Although these high-amplitude limit cycles are shown to be stable, from a hovering perspective, it is undesirable for a flapping robot. However, a discernible departure emerges beyond a critical frequency: Model B, characterized by the wing-wing interaction, exhibits reverse Hopf Bifurcation, a property that eludes Model A. It is noteworthy that both models share uniform attributes: the crank and rocker mechanism, wing geometry, and material composition. Consequently, the pivotal demarcation is attributed to the wing-wing interaction, which is enjoyed by Model B but not by Model A. In this context, the reverse bifurcation observed in Model B is attributed to the wing-wing interaction. It is possible that the transition from high amplitude oscillation to a fixed point is due to vibrational stabilization, as the flapping frequency at which this phenomenon occurs is 22 times the natural frequency of the system.

We also tested the recovery of Model B towards its stable equilibrium after applying different perturbations. These perturbations include a release from angular positions different from equilibrium values and impact perturbations imparted to both the body's initial angular velocity and translational velocity. The hovering point beyond the transition of Model B was robust enough to sustain a variety of perturbations with significant magnitudes. However, the response characteristics during recovery (e.g., settling time) were different for different perturbations, which points to the underpinning nonlinear dynamics of the system. This study unveils an interesting outcome that may be important for the design of flapping-wing robots. The wing-wing interactions promote passive stabilization of flapping robots, which may relax the stringent requirements of the flight controller and its actuators, making flapping robots more feasible and easier to design. Based on previous results in the literature of interacting wings aerodynamics that showed positive effects on thrust generation and handling self-induced vibrations, interacting wings seem to be an attractive design choice.

Acknowledgment

We would like to thank the National Science Foundation (NSF grant CMMI-1846308) for funding this research work.

We want to thank Asmaa Eldesoukey and Purshottam Verma for their valuable suggestions and help in the completion of the project.

Conflict of Interest

The authors declare that they have no financial, personal, or professional conflicts of interest that could have influenced the work reported in this manuscript. Each author confirms that there are no relationships with any entities in the public, private, or non-profit sectors that could be seen to influence the presented findings.

Data Availability Statement

The dataset used and/or analyzed during the current study is uploaded as additional materials.

References

Armanini S, Caetano J and De Croon Gea (2016) Quasi-steady aerodynamic model of clap-and-fling flapping mav and validation using free-flight data. *Bioinspiration and Biomimetics* 11(4): 046002.

Balta M, Deb D and Taha H (2021) Flow visualization and force measurement of the clapping effect in bio-inspired flying robots. *Bioinspiration and Biomimetics* URL `http://iopscience.iop.org/article/10.1088/1748-3190/ac2b00`.

Bennett L (1977) Clap and fling aerodynamics: An experimental evaluation. *Journal of Experimental Biology* 69(1): 261–272.

Berg JM and Wickramasinghe IM (2015) Vibrational control without averaging. *Automatica* 58: 72–81.

Berman G and Wang Z (2007) Energy-minimizing kinematics in hovering insect flight. *Journal of Fluid Mechanics* 582: 153–168. DOI:10.1017/S0022112007006209.

Bhatti M, Lee S and Han J (2021) Dynamic stability and flight control of biomimetic flapping-wing micro air vehicle. *Aerospace* 8(12): 362.

Bier M and Bountis T (1984) Remerging feigenbaum trees in dynamical systems. *Physics Letters A* 104(5): 239–244.

Bullo F (2002) Averaging and vibrational control of mechanical systems. *SIAM Journal on Control and Optimization* 41(2): 542–562.

Chen Z, Xie Y and Zhang Yea (2024) Aerodynamics of a flapping wing with stroke deviation in forward flight. *Physics of Fluids* 36(5).

Dawson S, Grebogi C and Yorke Jea (1992) Antimonotonicity: Inevitable reversals of period-doubling cascades. *Physics Letters A* 162(3): 249–254.

Deb D, Huang K and Fouda M (2022) *Effect of self-induced body vibrations on thrust generation in bio-inspired flying robots*. AIAA. DOI:10.2514/6.2022-0022. URL `https://arc.aiaa.org/doi/abs/10.2514/6.2022-0022`.

Deb D, Huang K and Verma Aea (2023) Thrust enhancement and degradation mechanisms due to self-induced vibrations in bio-inspired flying robots. *Scientific Reports* 13(1): 18317. DOI:10.1038/s41598-023-45360-4. URL `https://doi.org/10.1038/s41598-023-45360-4`.

Dhiman K, Abhishek and Kotharic M (2022) Flight dynamics and control of an unmanned helicopter with underslung double pendulum. *Journal of Aircraft* 59(1): 137–153.

Dickinson M, Lehmann F and Sane S (1999) Wing rotation and the aerodynamic basis of insect flight. *Science* 284(5422): 1954–1960.

Ellington C and Lighthill M (1984) The aerodynamics of hovering insect flight. iv. aerodynamic mechanisms. *Philosophical Transactions of the Royal Society of London. B, Biological Sciences* 305(1122). DOI:10.1098/rstb.1984.0052.

Ellington C, van den Berg C and Willmott Aea (1996) Leading-edge vortices in insect flight. *Nature* 384(6610): 626–630. DOI:10.1038/384626a0.

Hassan A and Taha H (2018) Combined averaging–shooting approach for the analysis of flapping flight dynamics. *Journal of Guidance, Control, and Dynamics* 41(2): 542–549.

Hassan A and Taha H (2019) Differential-geometric-control formulation of flapping flight multi-body dynamics. *Journal of Nonlinear Science* 29: 1379–1417.

Hong KS (2002) An open-loop control for underactuated manipulators using oscillatory inputs: Steering capability of an unactuated joint. *IEEE Transactions on Control Systems Technology* 10(3): 469–480.

Hopf E (1942) Abzweigung einer periodischen lösung von einer stationären lösung eines differentialsystems. *Berichte der Mathematisch-Physikalischen Klasse der Sächsischen Akademie der Wissenschaften Leipzig* 94: 1–22.

Jadhav S, Lua K and Tay W (2019) Effect of clap-and-fling mechanism on force generation in flapping wing micro aerial vehicles. *Bioinspiration and Biomimetics* 14(3): 036006.

Kapitza P (1951) Pendulum with vibrating suspension. *Uspekhi Fizicheskikh Nauk* 44(5): 7–20. DOI:10.3367/UFNr.0044.195105b.0007. URL https://ufn.ru/ru/articles/1951/5/b/.

Maggia M, Eisa S and Taha H (2020) On higher-order averaging of time-periodic systems: Reconciliation of two averaging techniques. *Nonlinear Dynamics* 99: 813–836.

Meerkov S (1980) Principle of vibrational control: Theory and applications. *IEEE Transactions on Automatic Control* 25(4): 755–762.

Phan H, Au T and Park H (2016) Clap-and-fling mechanism in a hovering insect-like two-winged flapping-wing micro air vehicle. *Royal Society Open Science* 3(12): 160746.

Ramananarivo S, Godoy-Diana R and Thiria B (2011) Rather than resonance, flapping wing flyers may play on aerodynamics to improve performance. *Proceedings of the National Academy of Sciences* 108(15): 5964–5969.

Sane S (2003) The aerodynamics of insect flight. *Journal of Experimental Biology* 206(23): 4191–4208. DOI:10.1242/jeb.00663.

Stephenson A (1908) On induced stability. *The London, Edinburgh, and Dublin Philosophical Magazine and Journal of Science* 15(86): 233–236. DOI:10.1080/14786440809463763. URL https://doi.org/10.1080/14786440809463763.

Taha H (2013) *Mechanics of flapping flight: Analytical formulations of unsteady aerodynamics, kinematic optimization, flight dynamics, and control*. Phd thesis, *Virginia Polytechnic Institute and State University*.

Taha H, Hajj M and Nayfeh A (2012) Flight dynamics and control of flapping-wing mavs: A review. *Nonlinear Dynamics* 70: 907–939.

Taha H, Hajj M and Nayfeh A (2014) Longitudinal flight dynamics of hovering mavs/insects. *Journal of Guidance, Control, and Dynamics* 37(3): 970–979.

Taha H, Kiani M and Hedrick Tea (2020) Vibrational control: A hidden stabilization mechanism in insect flight. *Science Robotics* 5(46): eabb1502.

Taha H, Kiani M and Navarro J (2018) Experimental demonstration of the vibrational stabilization phenomenon in bio-inspired flying robots. *IEEE Robotics and Automation Letters* 3(2): 643–647. DOI:10.1109/LRA.2017.2778759.

Taha H, Tahmasian S and Woolsey Cea (2015) The need for higher-order averaging in the stability analysis of hovering, flapping-wing flight. *Bioinspiration and Biomimetics* 10(1): 016002.

Taha H, Woolsey C and Hajj M (2016) Geometric control approach to longitudinal stability of flapping flight. *Journal of Guidance, Control, and Dynamics* 39(2): 214–226.

Tahmasian S and Woolsey C (2015) A control design method for underactuated mechanical systems using high-frequency inputs. *Journal of Dynamic Systems, Measurement, and Control* 137(7): 071004.

Taylor G, Nudds R and Thomas A (2003) Flying and swimming animals cruise at a strouhal number tuned for high power efficiency. *Nature* 425(6959): 707–711.

Vela P and Burdick J (2003) Control of underactuated mechanical systems with drift using higher-order averaging theory. In: *42nd IEEE International Conference on Decision and Control (IEEE Cat. No. 03CH37475)*, volume 3. pp. 3111–3117.

Zheng H, Xie F and Ji Tea (2020) Multifidelity kinematic parameter optimization of a flapping airfoil. *Physical Review E* 101(1): 013107.